REGULAR PAPER

Multi Element Diverging Beam from a Linear Array Transducer for Transverse Cross Sectional Imaging of Carotid Artery: Simulations and Phantom Vessel Validation

Akinlolu Ponnle, Hideyuki Hasegawa, and Hiroshi Kanai

REGULAR PAPER

Multi Element Diverging Beam from a Linear Array Transducer for Transverse Cross Sectional Imaging of Carotid Artery: Simulations and Phantom Vessel Validation

Akinlolu Ponnle[1], Hideyuki Hasegawa[2,1], and Hiroshi Kanai[1,2]*

[1]*Graduate School of Engineering, Tohoku University, Sendai 980-8579, Japan*
[2]*Graduate School of Biomedical Engineering, Tohoku University, Sendai 980-8579, Japan*

Transverse cross sectional imaging of the intima–media complex of the carotid arterial wall is difficult to obtain by conventional linear scanning. The angular widths of imaged regions of the anterior and posterior walls are limited. In this study, multi element diverging beam from a linear array transducer was investigated by simulations and experiments. B-mode image was reconstructed, using combinations of multi angle receiving beams from multiple transmissions per frame. The images obtained by the proposed method from simulations and silicone-rubber tube phantom showed an increase in the angular width over that in the case of conventional linear scanning. Also, images were investigated for sub aperture sizes of 36, 56, and 96 elements with different beam-spread angles. On the basis of the results of the present study, the sub aperture size of 36 elements and beam-spread angle of 90° are recommended for achieving the optimum results for this application in *in-vivo* imaging.

© 2011 The Japan Society of Applied Physics

1. Introduction

One of the main causes of cardiovascular disease is atherosclerosis and hence its diagnosis at an early stage has become very important.[1,2] A typical arterial wall consists of three layers: an innermost layer, "the intima"; a middle layer, "the media"; and an outer layer, "the adventitia".[3,4] The intima–media region of the artery is a useful place to probe in the diagnosis of atherosclerosis.[5–7] In a longitudinal cross sectional image obtained by conventional linear scanning, the anterior and posterior walls are displayed (double line pattern which represents echoes from the lumen–intima and media–adventitia boundaries),[6] but in transverse cross sectional imaging, the intima–media complex of the carotid arterial wall is difficult to image because reflection of ultrasound is highly angle-dependent,[8] and the ultrasound beams are perpendicular to the wall in a limited region. The *angular width* of this limited imaged region of the arterial wall is a measure of the extent of the anterior and posterior walls of the arterial cross section that are clearly imaged, if the transverse cross section of the arterial lumen is assumed to be circular. Intravascular imaging[9] has some practical drawbacks: it is invasive, expensive and can only be applied to patients that have already undergone surgical operation.[10,11] It is therefore clinically imperative for absolute diagnosis of the arterial wall to be able to visualize, noninvasively, the entire wall since any part of the wall (including side walls) could become defective but may not be imaged by conventional linear scanning.

Previous efforts to increase the angular width generally involves steering of focused transmit beams, as used in spatial multi angle compound imaging (MACI),[12] or specifically designing each scan beam to pass through the center of the artery over a limited region[13,14] or perpendicular to vascular walls at predetermined positions along the wall.[1] However, transmit steering angle is limited because of increase in the amplitude of grating lobes with steering. Also, in some cases, combination of multiple frames reduces the overall compound frame rate as well as producing temporal compounding in real-time applications, where the frame rate is the number of image frames displayed per second.

Although reduction in the overall frame rate or longer acquisition time for image reconstruction may pose no problem for static objects, it is a disadvantage for dynamic structures, for example, arterial vessels within the body.

The arterial vessel changes within one heart cycle. If MACI is employed, the overall frame rate decreases by a factor equivalent to the number of angular image frames that are compounded. For example, a typical scheme involves each spatial compound frame being produced from moving average of sequential frames. Averaging up to nine sequential frames typically improves the quality of the image in several ways, such as reduced speckle; reduced clutter caused by artifacts; and visualization of structures previously hidden beneath highly attenuating objects.[15] If each angular frame is acquired for a period of 10 ms, then the overall frame rate becomes 11.1 Hz (90 ms). The arterial vessel changes significantly within this period. The minimum arterial diameter, which corresponds to maximum intima–media thickness, is consistently located around the R wave of the electrocardiogram (ECG).[16] Apart from reduction of the overall compound frame rate, temporal compounding is also simultaneously performed, and this may result in the blurring of fast-moving objects in the field of view.[17] Therefore, there is a need to develop methods by which angular combination can be performed to reveal more features without extending the acquisition time or reducing the overall frame rate and/or if possible, increasing the overall frame rate.

The use of unfocused wide beams in transmit can increase the frame rate, for example, in parallel beamforming for fast imaging of the heart and artery.[18,19] In applications where frame rate is critical, ultrasound imaging techniques such as parallel receive beamforming,[20] explososcan[21] or ultrafast ultrasound imaging[22,23] are used. In these imaging techniques, the transmitted ultrasound beam is broader (slightly focused or plane waves) and it interrogates the entire volume of tissue. The backscattered ultrasound signal, received on the desired elements of the array transducer at once, is used to form several receiving beams or the entire ultrasound image. Ultrafast imaging is an extreme form of high-frame-rate imaging because, here, a plane wave is transmitted using the entire array transducer aperture and the echo signals are received using every element of the array transducer

*E-mail address: kanai@ecei.tohoku.ac.jp

© 2011 The Japan Society of Applied Physics

aperture at once.[24] However, in this application, the aforementioned techniques produce no significant improvement over unsteered focused beam of conventional linear scanning because the wavefronts of the transmit beams are all oriented in one direction spatially throughout the beam.

By using a diverging beam over a wide angle from a linear array transducer, a greater angular width of the imaged region can be obtained (and can increase with increasing number of transmissions) without steering of transmit beams and at the same frame rate as in conventional linear scanning. Also, the problem of receive grating lobes can be reduced (with improved resolution) by combining steered receiving beams from multiple transmissions.

A single element can produce a spherical wave if it is assumed to be a point radiator. Also, a sub aperture consisting of multiple elements can be used to emulate the radiation pattern of a virtual acoustic (point) source behind the transducer array.[25] This type of beam has previously been investigated by some researchers for diverse purposes. It was investigated by Karaman *et al.* using phased array transducers in synthetic transmit aperture (STA) imaging for small-scale systems,[26] by Lockwood *et al.* for sparse synthetic aperture systems with primary focus on three-dimensional (3D) ultrasound imaging,[27] and by Nikolov *et al.* for recursive STA imaging.[28] By properly delaying individual elements in the transmit sub aperture, good emulation of spherical waves diverging from the sub aperture surface can be obtained. An illustration of such a beam is shown in Fig. 1(a).

In this study, a wide-angled multi element diverging beam from a linear array transducer for transverse cross-sectional imaging of cylindrical vessels was investigated and images were reconstructed by combination of multi angle receiving beams from multiple sequential transmissions. Although receive beamforming from multiple transmissions increases the signal-to-noise ratio (SNR), its acceptance in many applications, particularly medical imaging is still limited.[26] By forming several steered receiving beams, one of the receive beams will pass through the center of the artery and thus be perpendicular to the arterial wall. By coherent combination of the multiple steered receiving beams (formed from several sequential transmissions stepped across the entire arterial cross section) at all image points of interest, a large angular width of the imaged region of the arterial wall could be obtained, thus eliminating the need for steering of transmit beams.

In the present study, acoustic field simulation and virtual scanning of a simulated "reflector tube" were performed using the Field II program.[29] Acoustic field measurement and scanning of a silicone-rubber tube phantom in water were also performed and the optimization of parameters was considered using results from simulations and phantom experiments.

2. Materials and Methods

2.1 Principle

2.1.1 Transmit beamforming and element time-delay calculation

In multi element diverging beam production, the excitation of each of the elements that make up the transmit sub aperture is time-delayed so that spherical resultant
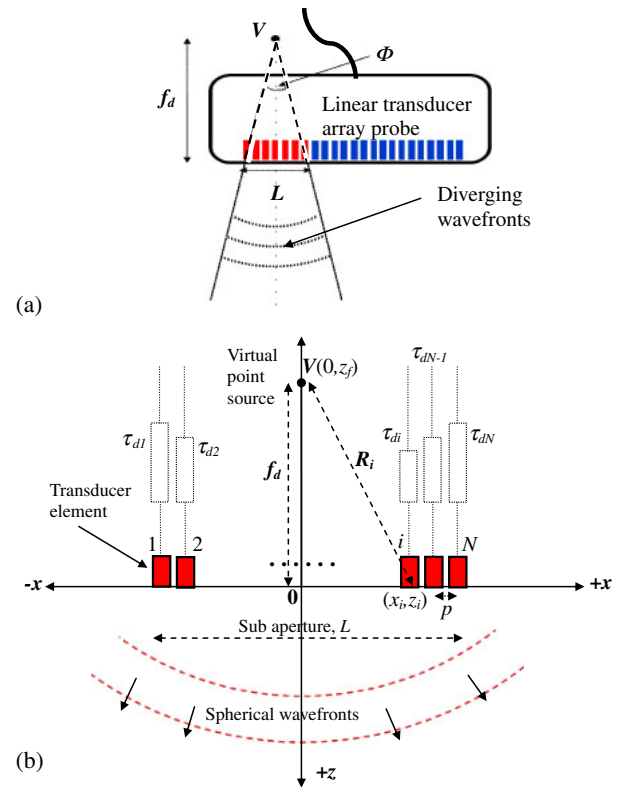

Fig. 1. (Color online) Multi element diverging beam from a linear array transducer. (a) Illustration of the beam. (b) Time-delay determination for each element of the transmit sub aperture. V is the virtual point source behind the array surface; f_d is the axial distance from the array surface to the virtual point source; L is the sub aperture length of N elements and Φ is the beam-spread angle (aperture angle or divergence angle).

wavefronts are produced in front of the transducer array over a limited angle. The time delays are governed by the location of the virtual point source with respect to the positions of the individual physical elements on the sub aperture. The time-delay calculation for each element is illustrated in Fig. 1(b) for an image plane on the x–z plane at $y = 0$ and a transmit sub aperture surface that lies along the x-axis with the sub aperture center at the origin $(0,0)$.

The time delay τ_{di} for a specific element, i ($i = 1, 2, 3, \ldots, N$), is calculated by

$$\tau_{di} = \frac{R_i - f_d}{c}, \tag{1}$$

where R_i is the distance from the virtual point source $V(0, z_f)$ to the center of element i, f_d is the axial distance from the array surface at $z = 0$ to point V and c is the speed of sound in the medium.

Virtual focal distance f_d is related to the beam-spread angle Φ and the transmit sub aperture length L by

$$f_d = \frac{L}{2 \tan(\Phi/2)}. \tag{2}$$

Sub aperture length L is related to the number of elements N in the transmit sub aperture by

$$L = p(N - 1), \tag{3}$$
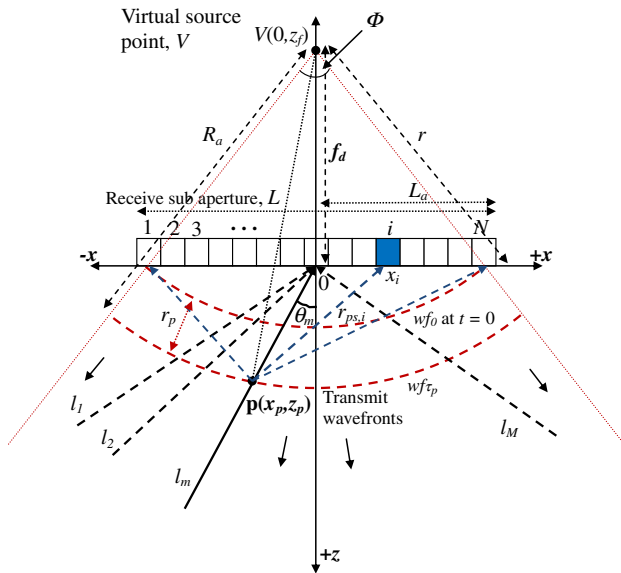
where p is the inter element pitch.

Fig. 2. (Color online) Receive steering and focusing on an image point within a transmit beam.

In terms of the coordinates,

$$\tau_{di} = \frac{1}{c}\left[\sqrt{x_i^2 + (z_f - z_i)^2} - z_f\right], \tag{4}$$

where x_i, z_i are the coordinates of the position of the center of element i.

Since the array surface lies along the x-axis [as shown in Fig. 1(b)], for each element i in the transmit sub aperture, $z_i = 0$. Therefore, x_i is expressed as

$$x_i = p\left[i - \left(\frac{N+1}{2}\right)\right], \tag{5}$$

and τ_{di} simplifies to

$$\tau_{di} = \frac{1}{c}\left(\sqrt{x_i^2 + z_f^2} - z_f\right). \tag{6}$$

In transmission, active sub apertures are stepped across the array at a pitch of one element with coincident transmit and receive sub apertures.

2.1.2 Receive beamforming

Since the beams are wide and can be assumed to be uniform, many steered receiving beams (or image lines) can be formed per transmission.[21] In any direction, the receive sub aperture must focus dynamically within the transmit beam. Focusing on an image point along a steered receiving beam within a transmit beam is illustrated in Fig. 2.

For a receive-focusing point (or image point) **p** at position (x_p, z_p) lying on receiving beam (or image line) l_m formed on the x–z image plane at $y = 0$ ($m = 1, 2, 3, \ldots, M$ where M is the total number of receiving beams formed for one transmit beam), the receiving beam is steered by the sub aperture through angle θ_m to receive-focus at **p**. The wf_0 is the wavefront at the beginning of reception ($t = 0$), and $wf\tau_p$ represents the wavefront that traverses point **p** at time $t = \tau_p$. If R_a is the radius of wavefront $wf\tau_p$ and r is the radius of wavefront wf_0, then the distance r_p (along the radial line joining point **p** to the virtual point source V) is

covered by the transmit wavefront to the image point **p** is given by

$$r_p = R_a - r. \tag{7}$$

Distance r is related to the receive sub aperture by

$$r = \sqrt{L_a^2 + f_d^2}, \tag{8}$$

where

$$L_a = p\left(\frac{N-1}{2}\right). \tag{9}$$

Also, R_a is related to point **p** by

$$R_a = \sqrt{x_p^2 + (f_d + z_p)^2}, \tag{10}$$

and time τ_p is

$$\tau_p = \frac{r_p}{c}. \tag{11}$$

Distance $r_{ps,i}$ covered by the scattered signal from point **p** to receive element i at point $[(x_i, z_i), z_i = 0]$, is given by

$$r_{ps,i} = \sqrt{(x_i - x_p)^2 + z_p^2}, \tag{12}$$

and time taken $\tau_{ps,i}$ is

$$\tau_{ps,i} = \frac{r_{ps,i}}{c}. \tag{13}$$

Total time of flight $t_{p,i}$ taken by ultrasound from the beginning of reception to reach receive element i via point **p** is given by

$$t_{p,i} = \tau_p + \tau_{ps,i} = \frac{r_p + r_{ps,i}}{c}, \tag{14}$$

Upon substituting eqs. (8), (10), and (12) into eq. (14),

$$t_{p,i} = \frac{1}{c}\left[\sqrt{x_p^2 + (f_d + z_p)^2} - \sqrt{L_a^2 + f_d^2} + \sqrt{(x_i - x_p)^2 + z_p^2}\right], \tag{15}$$

where element position x_i is determined using eq. (5).

Equation (15) describes the time at which the scattered signal from the image point, **p**, is received at the receive element i after reception commences at $t = 0$. Keeping the transmission fixed, eq. (15) determines which sample should be selected from among the sampled received signals to obtain a receive focus at the image point **p**.

If $y_{nt,i}(t)$ represents the received echo signal on element i for the nt-th transmission ($nt = 1, 2, 3, \ldots, N_T$, where N_T is the total number of transmissions per frame), the beam-formed image at point **p**, $s_{nt,l_m}(\mathbf{p})$ along the receive beam l_m is then given by

$$s_{nt,l_m}(\mathbf{p}) = \sum_{i=1}^{N} w_i y_{nt,i}(t_{p,i}), \tag{16}$$

where w_i is the apodization weight for element i.

2.1.3 Angular receiving beams combination from multiple transmissions

For one transmit beam from a transmit sub aperture, it is possible to form several steered receiving beams in
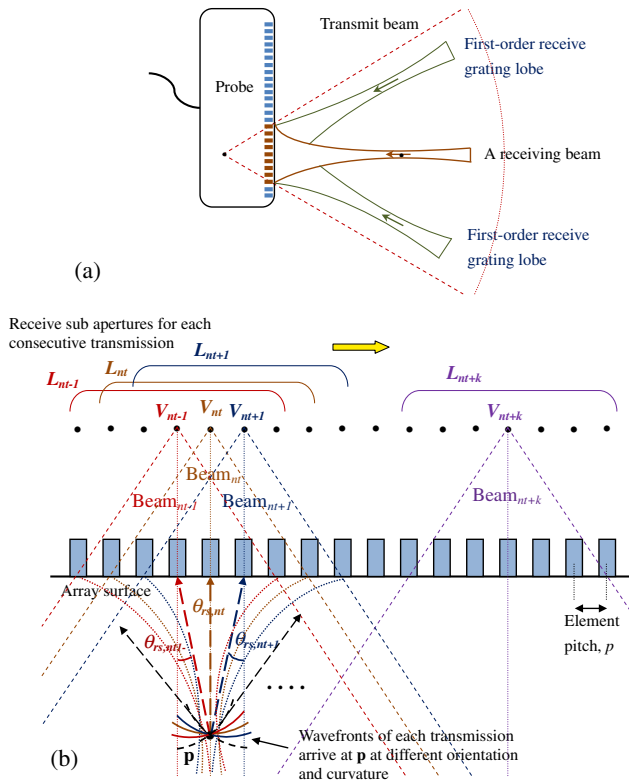
Fig. 3. (Color online) Receive-grating lobes and multiple steered receiving beams combination. (a) Illustration of first-order receive-grating lobes associated with a receiving beam. (b) Multiple steered receiving beams combination at point **p**, from transmissions in which transmit beam engulfs **p** and excludes others.

parallel.[21] In this work, several steered receiving beams within one transmit beam are formed in parallel. Corresponding steered receiving beams formed from each sequential transmit beam could be stacked to form an angular B-mode image. Many image frames (from different steered receive beams) could be combined to form a compounded image, as in MACI. However, because the transmit beam is wide and diverging, each receiving beam suffers from receive lateral sidelobes and receive grating lobes. Sidelobes and grating lobes are both unwanted parts of the ultrasound beam (off-axis) and may produce image artifacts as a result of error in positioning the returning echo.[30] Receive grating lobes associated with a receiving beam is illustrated in Fig. 3(a). If the separate angular B-mode images are averaged, the final compounded image would contain artifacts due to these lobes.

In order to reduce these effects, therefore, instead of combining the angular B-mode image frames formed from each steered receiving beam of each transmission, the focused RF signals $s_{nt,l_m}(\mathbf{p})$ [eq. (16)] of steered receiving beams from multiple transmissions at each image point of interest are summed. This is illustrated in Fig. 3(b). If the image point **p** is associated with a reflector, coherent summation will occur, resulting in a large beamformed signal, but for grating lobes and depth sidelobes, coherent summation will not occur. The intervals of the centers of transmit sub apertures is of one-element pitch. The transmit beam profile (for some beam-spread angle Φ) could be almost uniform within the beam but significantly low for

Table I. Parameters for the acoustic field simulation.

Transmit sub aperture size (elements)	96
Inter element pitch (mm)	0.2
Ultrasound transmit frequency (MHz)	7.5
Sampling frequency (MHz)	30
Assumed speed of sound in water (m/s)	1500
Assumed attenuation in water (dB/cm)	0.2170
Element excitation	Hanning-modulated sinusoid of two cycles
Transmit apodization	Boxcar
Beam-spread angle (deg)	86
Virtual source point	10 mm behind array surface

points outside the beam. The maximum steering angle of receiving beams in each transmit beam is limited to ±65° because of the limitation posed by the transducer array/ element directivity.

Therefore, in Fig. 3(b), the final beamformed image $S(\mathbf{p})$ at **p** is expressed as

$$S(\mathbf{p}) = \sum_{nt=1}^{N_{TP}} s_{nt,l_m}(\mathbf{p}), \qquad (17)$$

where N_{TP} is the number of transmissions for which point **p** lies within their transmit beams and having associated receiving beam with point **p** whose steered angle $\theta_{rs,nt}$ does not exceed the maximum receive steering angle. The N_{TP} is governed by the beam-spread angle Φ, the position of point **p** and the intervals of receive steering angles.

This method is utilized in order to be able to obtain the maximum possible angular width of the imaged region. Coherence summing of the RF signal at each image point from multiple transmissions is employed in synthetic aperture focusing technique (SAFT) and its variants, which provides very high resolution.[31,32] However, if SAFT is used in its classic form, the maximum angular width of the imaged region obtained would be less because, in this application, large beam-spread angle Φ and large transmit sub aperture size are used, so the region of interest (carotid arterial region which is at depths of 10 to 20 mm) therefore lies within the near field of the beam. Also, the use of synthetic transmit aperture (STA)[33] (which involves using all the elements in the entire transducer array to receive echo signals, thereby giving the highest image quality), would require a larger data memory and is more prone to motion artifacts, phase cancellation and speed errors at large receive-steering angles if the entire transducer array aperture is used for receive beamforming.

2.2 Simulations and experiments
2.2.1 Simulations
I Transmitted acoustic field
The acoustic field of the beam was simulated using the Field II program[29] with the simulation parameters listed in Table I. The program returns the values of the emitted pulsed pressure waves with time at all positions of interest within the beam. Specific depths of interest are 10, 15, and 20 mm.

Table II. Parameters for the virtual scanning.

Coincident transmit/receive sub aperture size (elements)	96
Inter element pitch (mm)	0.2
Transmit frequency (MHz)	7.5
Sampling frequency (MHz)	30
Assumed speed of sound in water (m/s)	1500
Assumed attenuation in water (dB/cm)	0
Transmit apodization	Boxcar
Receive apodization	Boxcar
Assumed frequency-dependent attenuation [dB/(m Hz)]	0
Element excitation	Hanning-modulated sinusoid of two cycles
Interval of centers of transmit sub apertures (mm)	0.2 (1-element pitch)
Number of transmissions for both scans	95
Mode of scanning for both scans	Linear sequential scanning
Transmit focus for the focused beam (mm)	14.1
Virtual source point for the diverging beam	10 mm behind the array surface

Fig. 4. (Color online) Schematic of the setup of the experimental system for the acoustic field measurement.

II   Virtual scanning of simulated "tube-shaped" reflector

Virtual (simulated) sequential linear scanning of a simulated "tube-shaped" reflector was also performed using the Field II program.[29] The transverse cross section of the "tube-shaped" reflector was simulated by dividing the walls into small point scatterers of equal strength with an inter scatterer spacing of 20 μm. The reflector has an inner radius of 4 mm and an outer radius of 5 mm with its center located at a depth of 14.1 mm below the transducer surface. The "simulated scanning" was performed by assuming the reflector to be in water with no attenuation with depth. Two separate "virtual" scans were performed using the transmit parameters in Table II. The first scan involves using unsteered focused beams, and in the second scan, diverging beams were used. The Field II program calculates and returns the values of the received RF signals (received voltage trace) for each of the elements in the receive sub aperture and for each transmission. These generated data were used for image reconstruction.

2.2.2   Experiments
I   Measurement of transmitted acoustic field

The acoustic field in water was measured using a hydrophone (Toray H025-002) in order to observe the pressure waveforms transmitted by the actual imaging system that we used. Figure 4 shows the schematic of the setup for the measurement of acoustic field using α-10 ALOKA ultrasound equipment with a 192-element linear array transducer of 10 MHz nominal frequency. The emission was set with an active transmit sub aperture of 96 elements and virtual acoustic source of 10 mm behind the array surface. No transmit apodization was used. The output from the hydrophone was amplified by the NF 5305 differential amplifier (DC-10 MHz) with a factor of 10, and the output from the amplifier was acquired with the TDS224 digital oscilloscope (Tektronix). Measurements were taken over a distance of 33 mm at intervals of 1 mm in the lateral
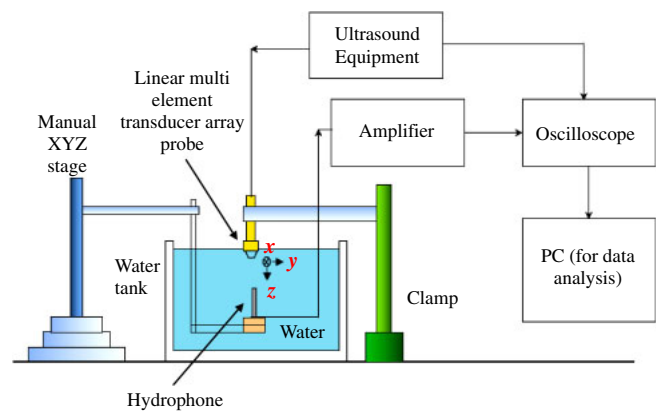
direction and at depths of 10, 15, and 20 mm below the transducer surface using a manual XYZ stage.

II   Transverse cross sectional scanning of silicone-rubber tube phantom in water

Transverse cross sectional scanning of a silicone-rubber tube phantom in water using the same ultrasound machine and transducer probe as described above was performed. The silicone-rubber tube phantom had an outer diameter of 10 mm and wall thickness of 1.0 mm. Its center was located at a depth of 14 mm below the transducer surface. Two separate scans were performed. In the first scan, unsteered focused beams with a focus at 14.1 mm were used and in the second scan, diverging beams with a virtual point source at 10 mm behind the array surface were used. The transmit/ receive sub aperture for each transmission is composed of 96 elements. The two scans were performed with 95 transmissions per frame at a frame rate of 109 Hz with an interval of centers of coincident transmit/receive sub apertures of one-element pitch. Received ultrasonic echoes were sampled at a frequency of 40 MHz. No transmit apodization was used. Received RF signals for each of the elements in the receive sub aperture and for each transmission were acquired for offline image reconstruction.

3.   Results
3.1   Acoustic field
3.1.1   Simulations

Figure 5(a) shows the simulated ultrasonic time-pressure waves at depths of 10, 15, and 20 mm below the transducer surface. From the figures, it can be seen that emulation of diverging waves is possible in the depth range from 10 to 20 mm, which corresponds to the typical depth of the carotid artery below the skin surface.

Figure 5(b) shows the time plot along the white lines in Fig. 5(a), for the waveform of the pressure waves that correspond to points at axial depths of 10, 15, and 20 mm below the center of the transmit sub aperture. The time axis in Figs. 5(a) and 5(b) is referenced to the time of the last element(s) to be fired, which in this case are the two extreme elements in the transmit sub aperture.

The middle plot of Fig. 5(b) shows the simulated emitted pressure waveform as it passes a point below the center of
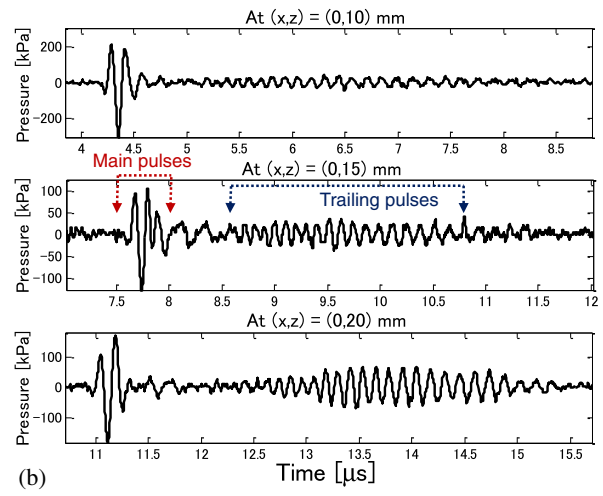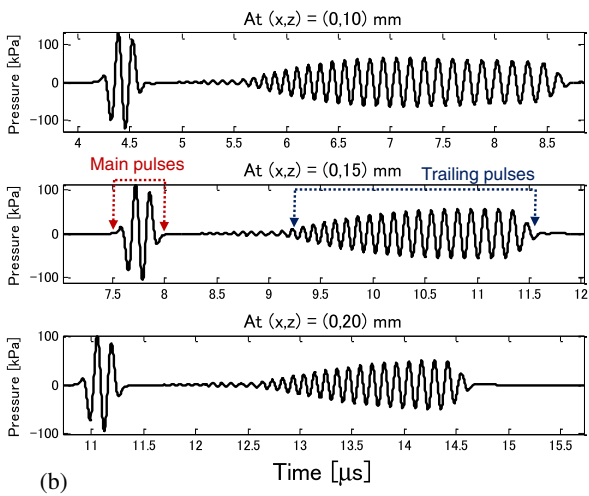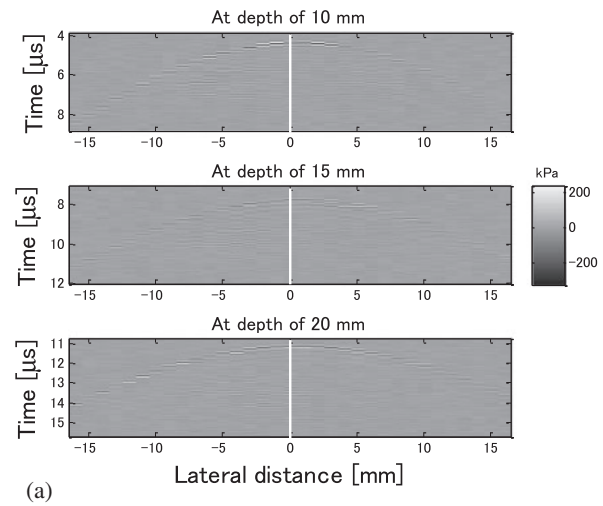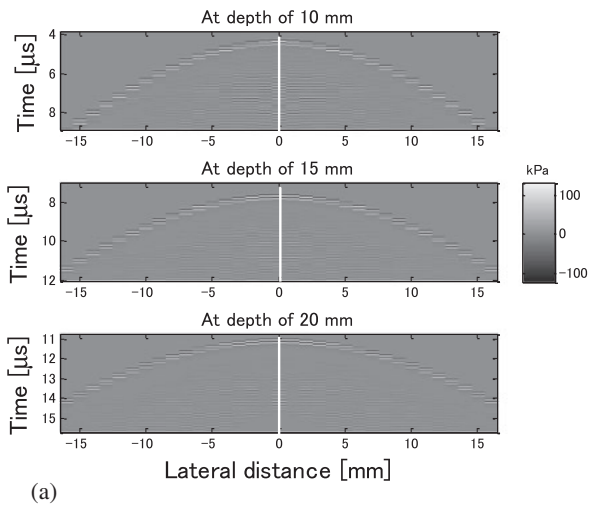
Fig. 5. (Color online) Simulated emitted waves. (a) At axial depths of 10, 15, and 20 mm. (b) Plots of the emitted waves along the white lines in (a).

Fig. 6. (Color online) Acoustic pressure as measured with the hydrophone. (a) At depths of 10, 15, and 20 mm. (b) Waveform of the RF signals along the white lines in (a).

the aperture at an axial depth of 15 mm. The emitted pressure waveform is a composite of two components: the main pulses and the trailing component. The main pulses are the resultant edge wavefront from the wavefronts of the individual elements and they are effective for imaging. The trailing component is the wavefronts (at a given position within the beam) resulting from the interference of delayed wavefronts which arrives at the point after the resultant edge wavefront has passed the point. Its length (spatial and temporal) and amplitude, which vary for different points within the beam, also depend on the number of elements, N, in the transmit sub aperture and the beam-spread angle, Φ. The trailing components cause temporal sidelobes (or depth sidelobes) in the image obtained using conventional receive beamforming, which may manifest as noise. It can also produce "ghost" structures in the image. With multiple transmissions and multi angle receive beamforming, such an effect is reduced.

3.1.2 Acoustic field measured with hydrophone

Figure 6(a) shows the amplified ultrasonic RF signals, acquired by the oscilloscope, from the hydrophone placed at depths of 10, 15, and 20 mm below the transducer surface.

In the figures, it can be seen that emulation of spherically diverging waves was achieved in the depth range from 10 to 20 mm, which corresponds to the typical depth of the carotid artery below the skin surface. Figure 6(b) shows the time plot of the waveform of the acquired RF signal along the white lines in Fig. 6(a), which correspond to points at axial depths of 10, 15, and 20 mm below the center of the transmit sub aperture.

Similarities can be seen between Figs. 5(a) and 6(a) as well as between Figs. 5(b) and 6(b). As the simulation result shows, the RF signals in Fig. 6(b) also contain two components: the main pulses and the trailing pulses. The time axis in Figs. 6(a) and 6(b) is referenced to the time of the last element(s) to be fired, which in this case are the two extreme elements in the transmit sub aperture.

3.2 Reconstructed images

Figure 7 shows the reconstructed B-mode images of the simulated tube-reflector obtained by simulated (virtual) scanning performed with the Field II program.[29] Boxcar apodization was used in receive. The angular width of the imaged region of the tube's anterior and posterior walls [illustrated in Fig. 7(b)] is wider in the image from the
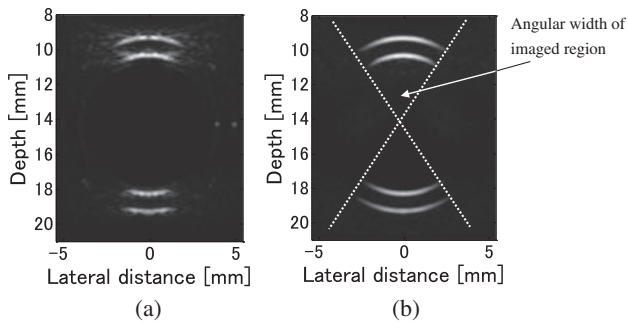
Fig. 7. Reconstructed B-mode images of the simulated tube-reflector. (a) Conventional linear scanning. (b) Proposed method.
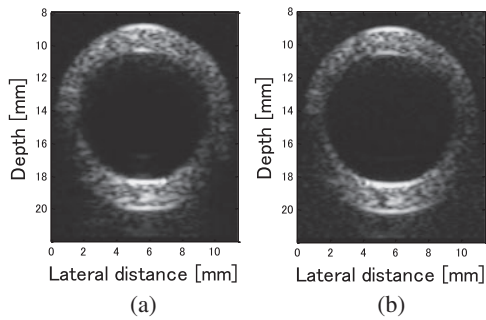

Fig. 8. Reconstructed B-mode images of the silicone-rubber tube phantom. (a) Conventional linear scanning. (b) Proposed method.

Fig. 9. B-mode images of the simulated tube reflector for different numbers of transmissions. (a) Conventional, focal distance of 14.1 mm. (b) Diverging beam scanning, virtual source distance f_d of 10 mm: (b-1) 29 transmissions, (b-2) 95 transmissions, (b-3) 157 transmissions with sub aperture of 36 elements and f_d of 4.1 mm.

Fig. 10. B-mode images of the simulated tube reflector at various receive steering angles. (a) $-15°$ receive-steering angle. (b) $0°$ receive-steering angle. (c) $+20°$ receive-steering angle. Artifacts due to receive lateral sidelobes, depth sidelobes and receive grating lobes can be seen in the images.

diverging beam than that in the image from the conventional focused beam. Figure 8 shows the reconstructed B-mode images of the silicone-rubber tube phantom. There is improvement in the lateral resolution in the reconstructed images using the diverging beam compared with that in reconstructed images using the conventional focused beam. For improved resolution and suppression of grating lobes and sidelobes, the minimum angular separation between the combined angular receive beams should be about 0.5°. A discrete angular interval of 0.5° was used in this study.

Figure 9 shows the reconstructed B-mode images obtained using focused beam and diverging beam for various numbers of consecutive sequential transmissions for the simulated tube reflector. It can be seen that a wider angle is obtained for 95 transmissions than that of 29 transmissions and a much wider angle is obtained for 157 transmissions using sub aperture size of 36 elements and $f_d = 4.1$ mm.

Increase in the angular width of the imaged region is possible with the diverging beam because by receive beamforming several angular beams within the transmit beams, at least one of the receive beams would pass through the center of the tube and thus be perpendicular to the tube wall. This part of the tube's surface will be different for different transmissions as they are stepped sequentially across the entire cross section. This is demonstrated in Figs. 10(a)–10(c), which are separate B-mode images (from simulation) formed with different angular receive beams. Each image is a partial view that does not portray the tube as a complete circular structure.
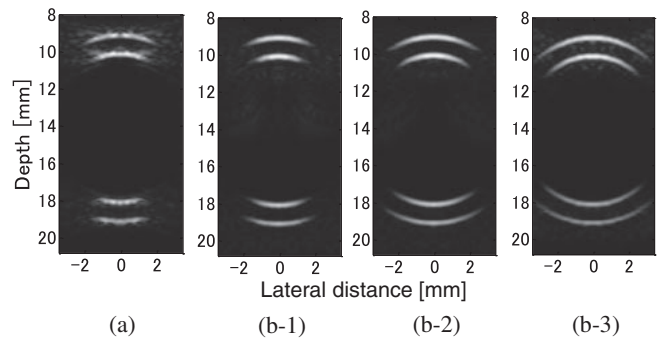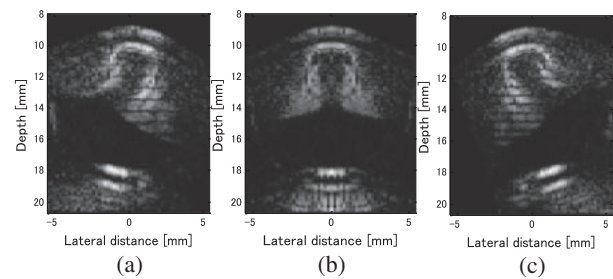
3.3 Optimization
3.3.1 Simulations
Figures 11(a)–11(d) show the B-mode images (from simulation) of the simulated tube reflector for beam-spread angles Φ of 86, 120, 150, and 180°, respectively for a sub aperture size of 96 elements and 97 transmissions. The plot in Fig. 12(a) shows the variation of the angular width of the imaged region (from simulated images) with different beam-spread angles Φ for three different sub aperture sizes of 36, 56, and 96 elements in comparison with the angular width obtained by focused beam scanning. The angular width increases with increasing Φ until about 120°, after which it decreases, and with increasing degradation in image quality. The worst image for all sub aperture sizes was obtained for $\Phi = 180°$. It should be noted that a 192-element linear array transducer was simulated, so different sub aperture sizes make it possible to achieve different maximum number of transmissions, N_{Tmax}, given by

$$N_{Tmax} = N_{e(total)} - N_{e(sub-aperture)} + 1, \qquad (18)$$

assuming the interval of centers of transmit sub apertures is of one-element pitch. The $N_{e(total)}$ is the total number of elements in the transducer array and $N_{e(sub-aperture)}$ is the number of elements in the transmit sub aperture. Applying eq. (18), for a sub aperture size of 96 elements, $N_{Tmax} = 97$; for a sub aperture size of 56 elements, $N_{Tmax} = 137$, and for a sub aperture size of 36 elements, $N_{Tmax} = 157$. Therefore,
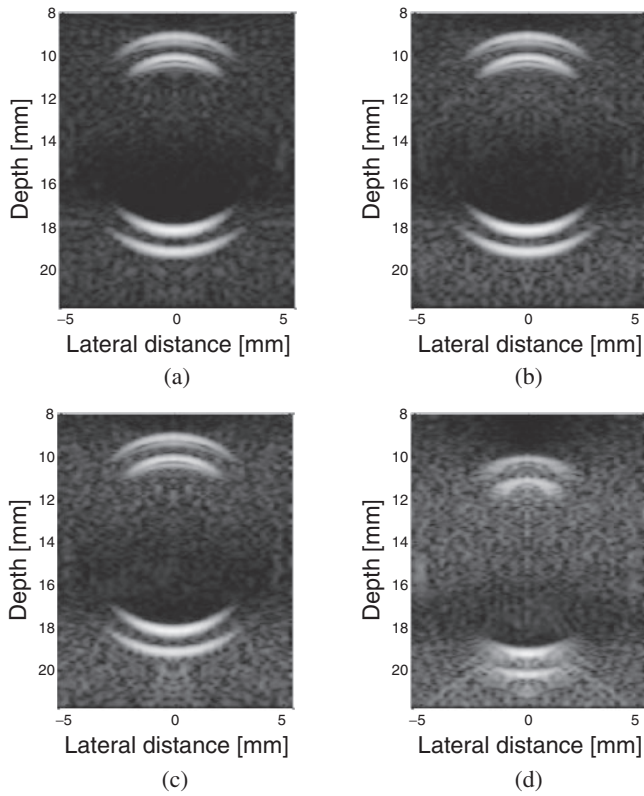
(a) (b) (c) (d)

Fig. 11. B-mode images (simulation) of the simulated tube reflector for a sub aperture size of 96 elements and 97 transmissions with beam-spread angles of (a) 86, (b) 120, (c) 150, and (d) 180°.
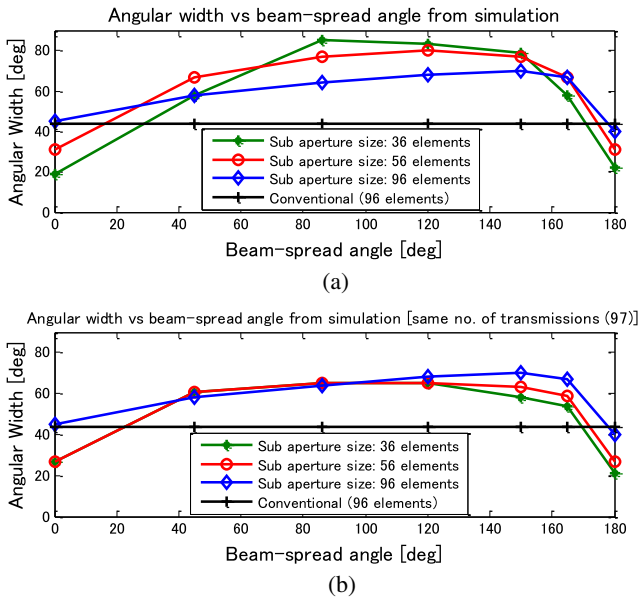

(a)

(b)

Fig. 12. (Color online) Variation of angular width of the imaged region (from simulated images) with different beam-spread angles, and coincident transmit/receive sub aperture sizes of 36, 56, and 96 elements: (a) maximum number of transmissions, (b) same number of transmissions (97).

the smaller the sub aperture size, the greater the number of possible transmissions and the wider the angular width becomes, provided the limit of the transducer's receive directivity is not yet reached.
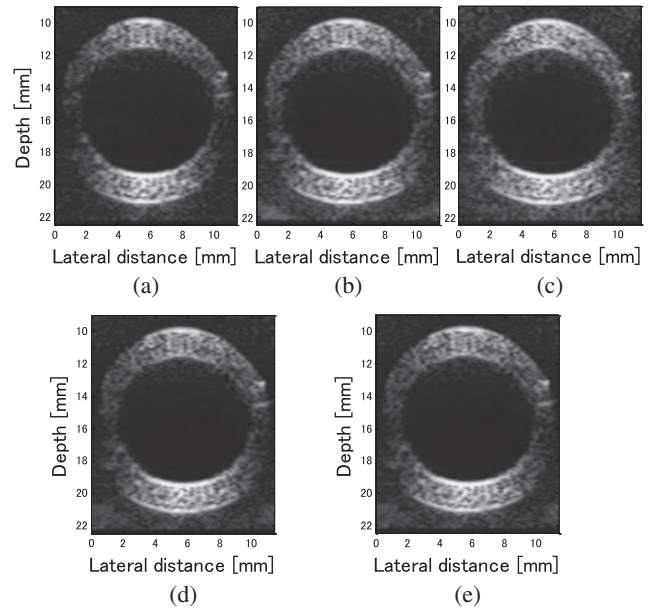

(a) (b) (c)

(d) (e)

Fig. 13. B-mode images of silicone-rubber tube phantom for different sub aperture sizes and different beam-spread angles Φ. (a) Φ of 87° and sub aperture size of 96 elements (97 transmissions). (b) Φ of 90° and sub aperture size of 56 elements (137 transmissions). (c) Φ of 90° and sub aperture size of 36 elements (157 transmissions). The sub apertures are coincident transmit/receive sub apertures. (d) and (e) correspond to (b) and (c), respectively, but with receive sub aperture size of 96 elements.

3.3.2 Phantom experiments

I   Angular width for different beam-spread angles and sub aperture sizes

Silicone-rubber tube phantom scanning was performed for different coincident transmit/receive sub apertures at different beam-spread angles. Figures 13(a)–13(c) show the B-mode images of the phantom for sub aperture sizes of 96 elements ($\Phi = 87°$), 56 elements ($\Phi = 90°$), and 36 elements ($\Phi = 90°$), respectively. Figure 14(a) shows the plot of the variation of the mean angular width of the imaged region with sub aperture sizes of 36, 56, and 96 elements at different beam-spread angles in comparison with the angular width obtained with conventional scanning. Since the imaged region that is observable is partly dependent on the image dynamic range, the mean value of observable angular width in images with dynamic ranges of 60, 50, and 40 dB was taken. From the plot in Fig. 14(a), the highest mean angular width is found to occur around Φ of 90 to 120° for all the three sub-apertures, and decreases with increasing Φ.

II   Contrast

The B-mode image contrast of the clearly imaged regions of the tube phantom was evaluated by considering the difference in signal level between the two regions indicated in Fig. 14(b). In the figure, region A is a clearly imaged region within the posterior wall of the tube phantom and region B is a region outside the posterior walls and tends to have significant noise levels.

The contrast ratio, CR, between the two regions is taken as

$$\mathrm{CR} = \frac{\mu_{\mathrm{A}} - \mu_{\mathrm{B}}}{\mu_{\mathrm{A}} + \mu_{\mathrm{B}}}, \qquad (19)$$
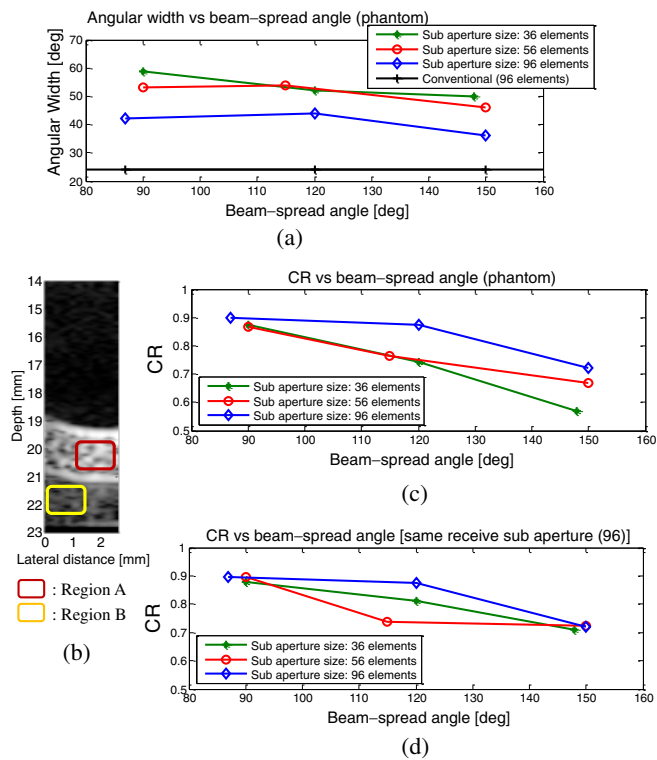
Fig. 14. (Color online) Optimization on the basis of phantom experiments for sub aperture sizes of 36, 56, and 96 elements. (a) Variation of mean angular width with beam-spread angle Φ. (b) Regions considered for CR evaluation. (c) Variation of CR for different Φ. (d) Variation of CR for receive sub aperture sizes of 96 elements for the three different transmit sub aperture sizes.

where μ_A is the mean signal level in region A, and μ_B is the mean signal level in region B. In eq. (19), CR of one (the maximum value) indicates the best contrast while CR of zero indicates the worst. Negative values of CR are most undesirable. The plot in Fig. 14(c) shows the CR obtained with different Φ and sub apertures sizes of 36, 56, and 96 elements. Sub aperture size of 96 elements has the highest CR at each Φ considered. Also, for each sub aperture, the highest CR occurs at Φ close to $90°$ and decreases with increasing Φ. At $\Phi = 90°$, the CR of the three sub apertures are relatively close.

The CR decreases with decreasing sub aperture size, because coincident transmit/receive sub aperture was used even though there is an increase in the number of transmissions with reduced sub aperture size. If the receive sub aperture size for each transmission of the three different transmit sub aperture sizes is retained at 96 elements, the CR would improve. Figures 13(d) and 13(e) are B-mode images of the phantom for transmit sub aperture sizes of 56 and 36 elements, respectively, but with a receive sub aperture size of 96 elements. Also, Fig. 14(d) shows the plot of the CR for a receive sub aperture size of 96 elements for all the three different transmit sub aperture sizes of 36, 56, and 96 elements. There is a relative increase in CR for the transmit sub aperture size of 36 elements at each Φ that was considered. For the transmit sub aperture size of 56 elements, there is also a relative increase in CR at $\Phi = 90$ and $150°$, but there is a slight decrease in CR at $\Phi = 120°$.

4. Discussion

As shown by the results, the angular width of the imaged region of the tube's wall increases with increasing number of transmissions when the proposed receive method is used with diverging beam. If the radius of curvature of the tube's wall is large relative to the wavelength, some parts of the tube's surface will be tangential to the diverging wavefronts of each linear sequential transmission (assuming consistency of wavefronts) depending on the relative position of the tube's wall within the beam of each transmission. These parts of the tube's surface are effective at specularly backscattering ultrasound to the receive sub aperture and are mainly the anterior and posterior walls of the tube. These regions act like an interface irrespective of the inter scatterer separation on the tube's wall, because of their almost perpendicular orientation to the ultrasonic transmit beams for most of the transmissions. It is the extent of these regions that can increase when imaged with diverging transmit beam and with greater number of linear sequential transmissions, though it would be limited by the attenuation of the echo signals with increasing distance, array receive-steering/ element directivity, time gain compensation (TGC), and maximum number of available transducer elements in the linear transducer array probe.

If the linear sequential transmissions are symmetrically stepped (about the tube's center) across the tube cross section, the angular width of the imaged region of the anterior and posterior parts of the tube's wall would have equal half-angles.

The region of the two side walls of the simulated tube reflector is negligibly visible in Fig. 7, but it can still be seen in the phantom image in Fig. 8 because of scattering within the phantom wall. For the simulated tube reflector, only two widely separated reflecting walls are assumed. Therefore, the two side walls cannot be imaged by *specular reflection* alone as the angle of the reflected echoes are so large that they slide off the receive sub aperture for most of the transmissions. This region of the two side walls is also difficult to image with focused beam.

Imaging of the region of the two side walls strongly depends on the scatterers backscattering ultrasound to the receive sub aperture. This is demonstrated in the phantom experiment. Since the scattering of ultrasound by point scatterers is isotropic, this region is expected to be easily imaged. However, scatterers on the sidewalls (and within the thickness of the sidewalls) both in phantoms and in tissues are randomly placed with random scattering amplitudes and random phases. Therefore, the summed scattered waves (interference of echoes) from the scatterers may experience either constructive interference or destructive interference depending on the relative phases of the scattered waves which, among other factors, is influenced by the relative positions of the scatterers and the transmit beam wavelength. If there is constructive interference, the side walls can be seen.

From the simulation result of the optimization of parameters; it can be seen that for all the three sub-apertures simulated, the optimum result lies within beam-spread angle Φ of 86 to $150°$. Smaller sub aperture size tends to produce greater angular width, but correspondingly, the contrast

© 2011 The Japan Society of Applied Physics

suffers. Also, if Φ increases beyond $150°$, the beam is no longer uniform and the ratio of the maximum amplitude of the trailing pulses to the maximum amplitude of the main pulses significantly exceeds one (1) within the beam. The phantom results show that contrast ratio CR decreases with increasing Φ and the angular width remains fairly constant within 90 and $120°$ but decreases rapidly thereafter. With an equal receive sub aperture size of 96 elements, the CR improved.

Frame rate also decreases with decreasing sub aperture size owing to an increase in the number of possible maximum transmissions. Therefore, recommended parameter values are a sub aperture size of 36 elements and Φ of $90°$. This combination is expected to yield optimum results in *in vivo* experiments.

5. Conclusions

In this study, it has been demonstrated, through simulations and silicone-rubber tube phantom experiments, that transverse cross sectional image of cylindrical vessels could be obtained over wider regions than is possible with conventional linear scanning as a result of employing multi element diverging beams from a linear array transducer. This strategy eliminates steering of transmit beams and the same frame rate as in conventional linear scanning is still retained by combining multiple angular receiving beams from multiple sequential transmissions of the same frame. However, since the beams are spherically wide, there is a more stringent requirement on the receive beamformer to be less sensitive to receive sidelobes and grating lobes, as well as to avoid lateral spatial under-sampling because of grating lobe artifacts.

Also, this study revealed that optimized beam parameters are a sub aperture size of 36 elements and beam-spread angle Φ of $90°$. The proposed method is intended to be applied to *in vivo* transverse cross sectional scanning of carotid arteries.

1) T. Mashiyama, H. Hasegawa, and H. Kanai: Jpn. J. Appl. Phys. **45** (2006) 4722.
2) K. Ikeshita, H. Hasegawa, and H. Kanai: Jpn. J. Appl. Phys. **48** (2009) 07GJ10.
3) D. Valdez-Jasso, H. T. Banks, M. A. Haider, D. Bia, Y. Zocalo, R. L. Armentano, and M. S. Olufsen: Adv. Appl. Math. Mech. **1** (2009) 151.
4) G. A. Holzapfel, T. C. Gasser, and R. W. Ogden: J. Elasticity **61** (2000) 1.
5) A. D. M. Van Swijndregt, E. E. de Lange, E. de Groot, and R. G. A. Ackerstaff: Ultrasound Med. Biol. **25** (1999) 323.
6) A. D. M. Van Swijndregt, S. H. K. The, E. J. Gussenhoven, C. T. Lancee, H. Rijsterborgh, E. de Groot, A. F. W. van der Steen, N. Bon, and R. G. A. Ackerstaff: Ultrasound Med. Biol. **22** (1996) 1007.
7) H. Hasegawa and H. Kanai: IEEE Trans. Ultrason. Ferroelectr. Freq. Control **55** (2008) 1921.
8) K. Kudo, H. Hasegawa, and H. Kanai: Jpn. J. Appl. Phys. **46** (2007) 4873.
9) P. G. Yock and D. T. Linker: Circulation **81** (1990) 1715.
10) C. L. de Korte, M. Sirevogel, F. Mastik, C. Strijder, E. Velenan, G. Pasterkamp, and A. F. W. van der Steen: Circulation **105** (2002) 1627.
11) H. G. Hansen, R. G. P. Lopata, and C. L. de Korte: IEEE Trans. Med. Imaging **28** (2009) 872.
12) S. K. Jespersen, J. E. Wilhjelm, and H. H. Silleson: Ultrason. Imaging **20** (1998) 81.
13) N. Nakagawa, H. Hasegawa, and H. Kanai: Jpn. J. Appl. Phys. **43** (2004) 3220.
14) K. Kudo, H. Hasegawa, and H. Kanai: J. Med. Ultrason. **34** (2007) 23.
15) F. W. Kremkau: *Diagnostic Ultrasound: Principles and Instruments* (Saunders Elsevier, Philadelphia, PA, 2006) 7th ed., p. 114.
16) R. H. Selzer, W. J. Mark, P. L. Lee, H. Kwong-Fu, and H. N. Hodis: Atherosclerosis **154** (2001) 185.
17) T. L. Szabo: *Diagnostic Ultrasound Imaging: Inside Out* (Academic Press, Boston, MA, 2004) p. 327.
18) H. Hasegawa and H. Kanai: Proc. 30th Symp. Ultrasonic Electronics, 2009, p. 401.
19) H. Hasegawa and H. Kanai: IEEE Trans. Ultrason. Ferroelectr. Freq. Control **55** (2008) 2626.
20) M. O'Donnell: Proc. IEEE Ultrasonics Symp. 1990, Vol. 3, p. 1495.
21) D. P. Shattuck, M. D. Weinshenker, S. W. Smith, and O. T. von Ram: J. Acoustic Soc. Am. **75** (1984) 1273.
22) B. Delannoy, R. Torquet, C. Bruneel, E. Bridoux, J. M. Rouvaen, and H. Lasota: J. Appl. Phys. **50** (1979) 3153.
23) M. Fink, L. Sandrin, M. Tanter, S. Catheline, S. Chaffai, J. Bercoff, and J. Gennisson: Proc. IEEE Ultrasonics Symp., 2002, Vol. 2, p. 1811.
24) S. Park, S. R. Aglyamov, W. G. Scott, and S. Y. Emelianov: IEEE Trans. Ultrason. Ferroelectr. Freq. Control **54** (2007) 987.
25) K. Gammelmark and J. A. Jensen: IEEE Trans. Med. Imaging **22** (2003) 552.
26) M. Karaman, P. Li, and M. O'Donnell: IEEE Trans. Ultrason. Ferroelectr. Freq. Control **42** (1995) 429.
27) G. R. Lockwood, J. R. Talman, and S. S. Brunke: IEEE Trans. Ultrason. Ferroelectr. Freq. Control **45** (1998) 980.
28) S. I. Nikolov, K. Gammelmark, and J. A. Jensen: Proc. IEEE Ultrasonics Symp. 1999, Vol. 2, p. 1621.
29) J. A. Jensen: Med. Biol. Eng. Comput. **34** (1996) Suppl. 1, Part 1, p. 351.
30) P. Y. Barthez, R. Leveille, and P. V. Scrivani: Vet. Radiol. Ultrason. **38** (1997) 387.
31) R. N. Thomson: Ultrasonics **22** (1984) 9.
32) J. A. Jensen, S. I. Nikolov, K. L. Gammelmark, and M. H. Pedersen: Ultrasonics **44** (2006) e5.
33) M. Nikolov and V. Behar: Cybern. Inf. Technol. **5** (2005) 53.